Analysis of Aerodynamics in Northern Flying Squirrel Patagium: 3D Printing, Experimental Flow Visualization, and Computational Fluid Dynamics

Zackary Tileston

Professors: Laura Miller & Matea Santiago

Course: MATH 481 Fall 2023

University of Arizona

Abstract

This study investigates the aerodynamics of the northern flying squirrel's patagium, providing insights into natural gliding mechanisms and their implications for the design of multimodal robotics. Utilizing 3D-printed models and computational fluid dynamics, the research explores the impact variations in the angle of attack on aerodynamic performance, specifically lift and drag forces. The hypothesis centers on identifying an optimal angle range that maximizes lift while minimizing drag, thus enhancing aerodynamic efficiency. Results indicate a significant relationship between angle of attack and lift-to-drag ratio, offering valuable data for multi-modal robotic applications.

Introduction

Northern flying squirrels possess a unique ability among the animal kingdom of actively controlling their descent, or gliding. The patagium is the skin membrane responsible for giving them their ability to glide. Encyclopædia Britannica provides this general information as well as a diagram showing the patagium in Fig. 1 [7]. The gliding mechanics of these squirrels, as described by Bishop, illustrates the importance of aerodynamics in natural gliders [8]. There is a unique opportunity to improve the field of robotics through analysis of these gliding mechanisms found in nature. Obtaining a better understanding of how squirrels glide can help inform the design of multi-modal robots that possess an on-land propulsion system as well as the ability to glide. This will allow for robots to make descents without the restrictions and added complexity of traditional flying robots as laid out by Leutenegger et al. [15].

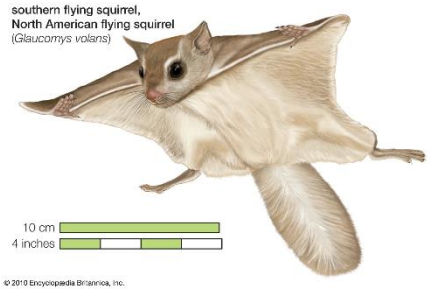


Figure 1: Diagram of southern flying squirrel. The patagium can be seen stretched between the arms and legs [7].

Previous research primarily explored the creation and analysis of artificial prototype robotics and not the patagium of live specimen. Li et al. focused on studying variations in environmental conditions and their influence on dynamic gliding behaviors [3]. In a study sharing some of the same authors, further developments in this field expanded the scope to include the relationship between membrane flexibility and its impact on aerodynamic forces [2]. Unlike the referenced studies, which primarily focus on the overall aerodynamic effects of active membrane deformation in robotic flying squirrels, I will investigate the specific impact of angle of attack on lift and drag forces in models analogous to actual flying squirrels as opposed to robotic recreations. By varying the angle of attack in both a physical model and computational simulations, I aim to uncover detailed insights into how these adjustments affect aerodynamic performance. This is particularly important for the design of robotics that need to transition smoothly between different modes of movement, such as from climbing to gliding. I hypothesize that varying the angle of attack in these modes will significantly influence the lift-to-drag ratio. Specifically, there exists an optimal range of angles that maximize lift while minimizing drag, thereby enhancing the aerodynamic efficiency and maneuverability of the flying squirrel. In this study, I will identify the range in which performance of multi-modal robots is optimized. Furthermore, I suspect I will find a positive relationship between the angle of attack and lift coefficient similar to the model used by Li et al. [3].

Within the methods section of this paper, I will describe the process of preparing and analyzing a 3D model of a northern flying squirrel for both physical flow visualization and computational fluid dynamics simulations. This will include the specifics of model preparation, the setup for the flow tank experiment, and the parameters for the CFD simulations. The results section will show the values received from the CFD simulation as well as analysis of photographs from the flow visualization. Lastly, the discussion will interpret the results and relate them to my thesis statement.

Methods

The 3d model for the northern flying squirrel was obtained from Printables user @Schlossbauer [4]. Since the model was originally made for decorative purposes, changes needed to be made to make it compatible with the ANSYS CFD software package [11]. To do so, the model was edited in Autodesk Meshmixer [12]. The squirrel model originally contained a hole made for a stand that needed to be filled in and smoothed to resemble the abdomen of a live specimen. Additionally, the model was smoothed, reduced, and remeshed within Meshmixer [12]. This was done to lower the number of triangles in the model and therefore reduce the computation time required in ANSYS [11]. The model was then further improved within ANSYS Spaceclaim by using the software to check for and fix any errors in the model geometry [11]. The model for 3D printing and the CFD simulation are the same except that the 3D printed model retained the stand hole that was removed in the simulation model. Both are roughly the size of the average northern flying squirrel and are 69.0 X 107.1 X 34.7 mm in the X, Y, and Z directions. In addition to the flying squirrel, 5 stands were designed, each with a different angle of attack: 25°, 7°, 0°, -11°, and -29°. The stands were constructed in the 2023 Professional version of Autodesk Inventor [16]. The final model used in the simulation is depicted in Fig. 2.

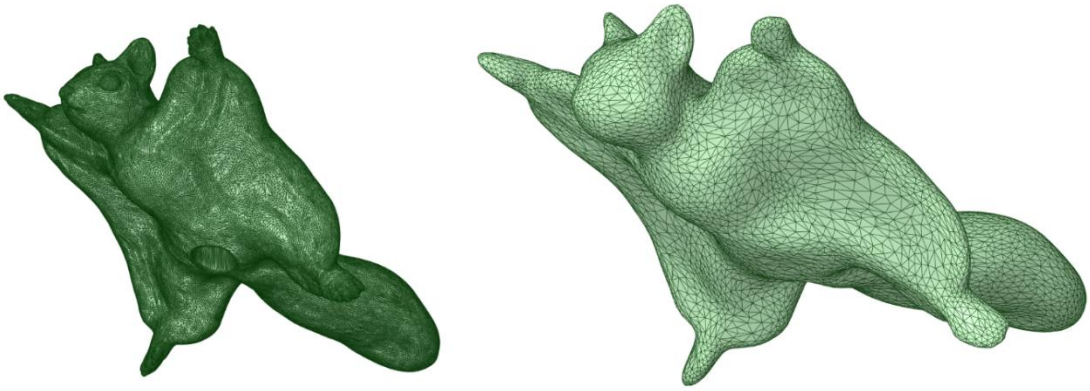


Figure 2: (Left): Unedited original model. (Right): 3D model used for printing and CFD simulation.

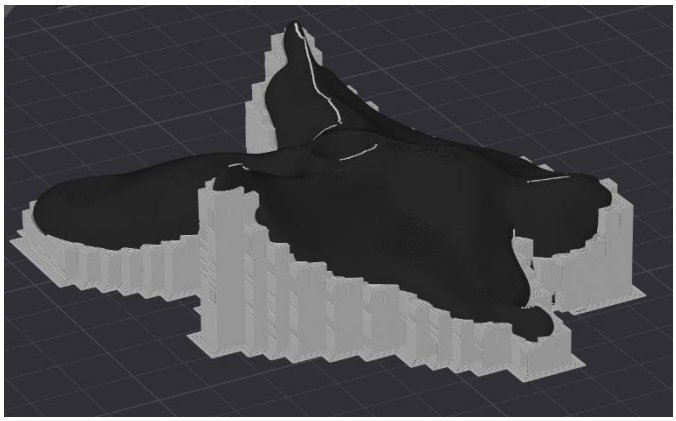


Figure 3: 3D model in slicer before printing. PLA plastic shown in black and water soluble PVA material shown in white.

After the final model was made, it was 3D printed using my personal 3D printer – a Bambu Lab X1-Carbon. Before being printed the model needed to be prepared using the Bambu Studio slicer, a software that translates the model file into machine instructions [17]. Since the 3D printed part will be used in a physical flow simulation, the slicing settings were adjusted to make the print as smooth as possible. It was printed with a very fine resolution at 0.08mm layer height and water-soluble supports were used to avoid defects caused by printing overhangs with traditional support material. The model was also oriented with the stomach facing upwards to give it the smoothest finish. The model can be seen in the slicer before printing in Fig. 3 and after printing in Fig. 4. Next, the printed model was post-processed to prepare it for flow visualization. The support material was first removed by dissolving it in water. Then to further smooth the printed part, it was sanded and painted using black Rust-Oleum enamel spray paint. Finally, the 5 stands were printed, each with 100% infill to make the parts less buoyant.



Figure 4: Final model after being smoothed and painted.

With the model fully prepared, it was now time for the flow visualization. The model was set inside a flow tank provided by the University of Arizona mathematics department. The tank as pictured in Fig. 5 was made to Vogel and LaBarbera's specifications [18]. Marine putty was used to attach the squirrel model to the stands and to fix the stands to the bottom of the tank. The motor was set to 14% of its max RPM to simulate a turbulent flow and still provide a clear visualization. To find the velocity of the water a video was taken of a blob of fluorescence dye passing over a ruler placed alongside the tank. It took the dye 6 seconds to travel 30 cm, giving the water a velocity of 0.05 m/s.

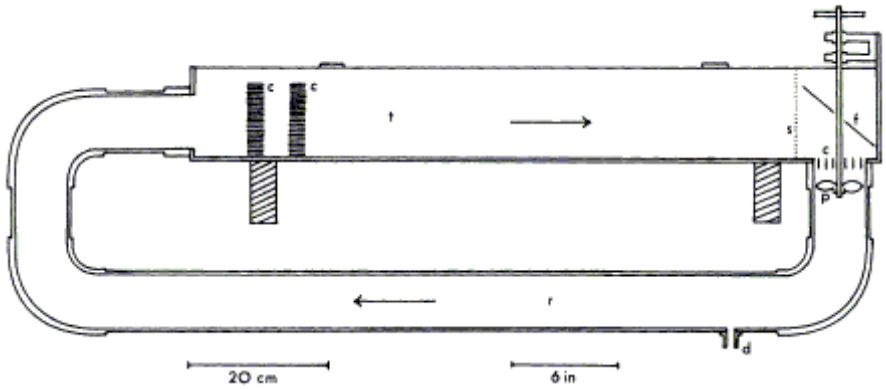


Figure 5: Diagram of tank used for flow visualization, image from [18]. Tank has dimensions of 100 X 10.7 X 12.9 cm.

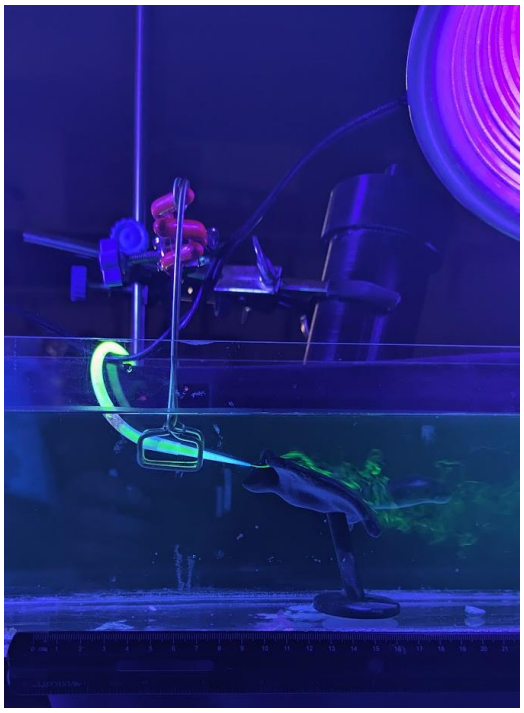


Figure 6: Flow visualization setup using a Mariotte bottle

A Mariotte bottle was placed in front of the patagium to dispense fluorescence dye at a constant flow rate and held by clamps attached to a pole outside of the tank. Two UV lamps were placed facing the model from different directions and the lights in the room were shut off, causing the dye to fluoresce. Video footage was obtained using a smartphone mounted on a tripod facing the tank. The setup is depicted in Fig. 6. Recordings were shot for each of the 5 angled stands. The water in the tank was emptied and replaced as needed when dye oversaturated the water.

The ImageJ software package was used to analyze images taken from the video [19]. This software enabled me to measure the wake and leading edge vortex of the flow in the tank. This will be used to cross-reference the computational fluid dynamic simulation to ensure it is consistent with the experimental results.

To compare with the CFD simulation, the Reynold's number is calculated for both the water tank and simulation fluid domain. Equation 1 is used for finding the Reynold's numbers, where ρ is the density of the fluid, U is the flow velocity, L is the characteristic length, and μ is the dynamic viscosity.

$$R_e = \frac{\rho U L}{\mu} \tag{1}$$

Starting with the flow visualization, the density of tap water is 997.88 $\frac{Kg}{m^3}$ [13]. The velocity was found above to be 0.05 $\frac{m}{s}$. The characteristic length is 0.22 m [6]. Lastly, the dynamic viscosity (at an assumed temperature of 20° C) is 0.001 $\frac{Ns}{m^2}$ [14]. These values are all plugged into Equation 1 to give a Reynold's number of 10,977.

Equation 2 is used to calculate the Reynold's number for the CFD simulation, due to being unable to find a source for the dynamic viscosity. The equations are equivalent in usage.

$$R_e = \frac{UL}{V} \tag{2}$$

Here, V represents the kinematic viscosity, the value for which is 1.4621 X 10^{-5} $\frac{m^2}{s}$ [5]. The same characteristic length from the flow visualization is used for the CFD, 0.22 m [6]. The flow velocity is set to the average gliding speed of 8 $\frac{m}{s}$ found by Zhao et al. [6]. Finally, the Reynold's number is calculated and gives a value of 120,375.

Both numbers are above 3,500 and therefore exhibit turbulent flow, however they differ by an order of magnitude, meaning they will not be in the same regime. This large discrepancy comes from limitations in the flow tank design. The tank is made to show flow through using a

high contrast fluid but cannot quantitatively determine air flow. However, this will still be useful for qualitative discussion later.

To create the CFD simulation the 2023 R2 Student version of ANSYS Fluent was used [11]. This program uses the Navier-Stokes equations to simulate fluid flow. A steady flow is assumed to put the equations in a simplified form:

$$\rho(u \cdot u\nabla)u = -\nabla p + \mu\Delta u + f \tag{3}$$

$$\nabla \cdot u = 0 \tag{4}$$

In the above equations, ρ is the density of the fluid (air in this case), u is the fluid velocity, ∇ is a gradient operator, p is the pressure, μ is the dynamic viscosity of the fluid, and f represents the forces acting on the fluid. Since the Reynold's number is above 3,500, the simulation is firmly in the turbulent flow domain. Because of this, a RANS model was used to approximate the Navier-Stokes equations, specifically the k-omega SST formulation.

As mentioned above, the model was first refined and checked for errors using ANSYS SpaceClaim [11]. Next, the boundary conditions for the simulation needed to be set within ANSYS Mesh [11]. A box was built by Professor Santiago around the model with 2L in front of the squirrel, 2L on either side, L on top and bottom, and 5L behind the squirrel, where L is the characteristic length typical of flying squirrels as used previously [6]. Next, the mesh was created using 3 inflation layers and adaptive sizing with a resolution of 2. The final mesh contained 999,470 elements and had a minimum orthogonal quality of 0.11524. The element size was 0.007 m. Overall dimensions were 0.42 X 1.28 X 0.37 m. The mesh can be viewed in Fig. 7, with the inlet being set to the leftmost face and the outlet being set to the rightmost face.

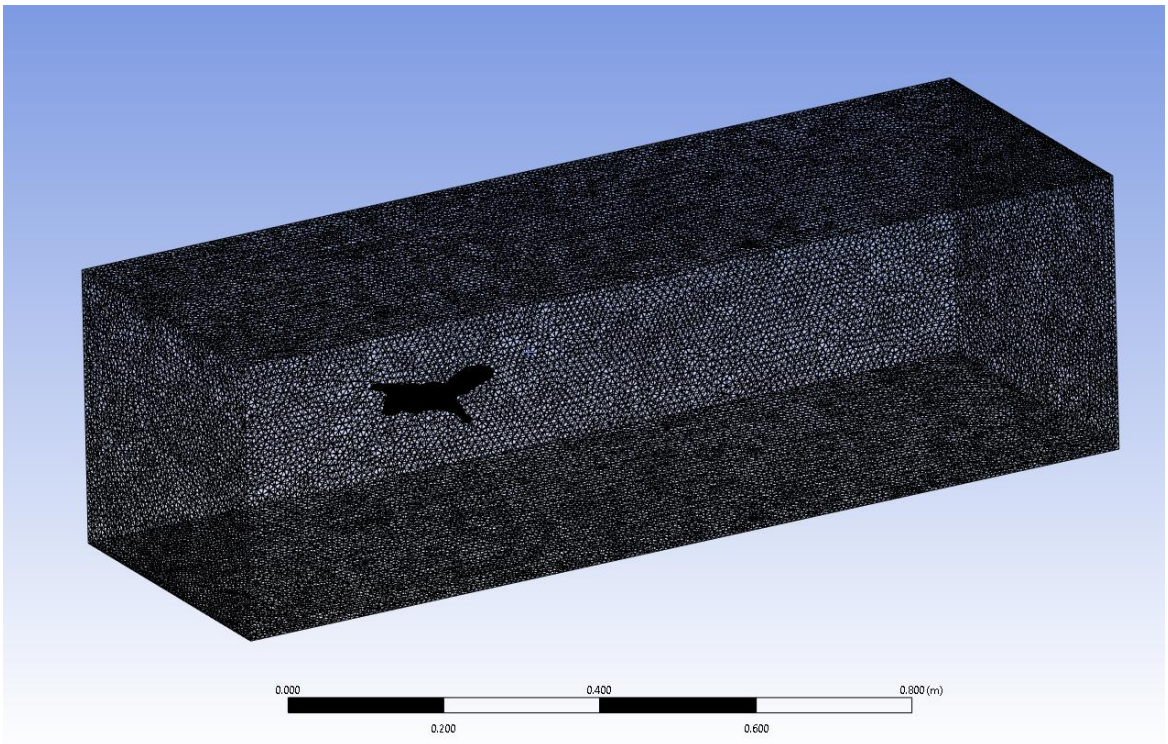


Figure 7: Boundary conditions and final mesh

Now ANSYS fluent can be used to simulate the flow around the model [11]. The density and fluid velocity were set to match what was used to calculate the Reynold's number in equation 2. Likewise, the model was scaled to match the characteristic length in equations 1 and 2. Report definitions were made to calculate the lift and drag forces and coefficients. Residuals were set to converge at values under 10^{-3}. Finally, the calculation was run with a time scale of 0.05. Two additional simulations were run to vary the angle of attack. In total, three attack angles were simulated: -15°, 0°, and 15°. I created the simulation for the 0° angle and Professor Miller aided in running the simulations for the other two angles. The residuals for the 0-degree attack angle are shown in Fig. 8.

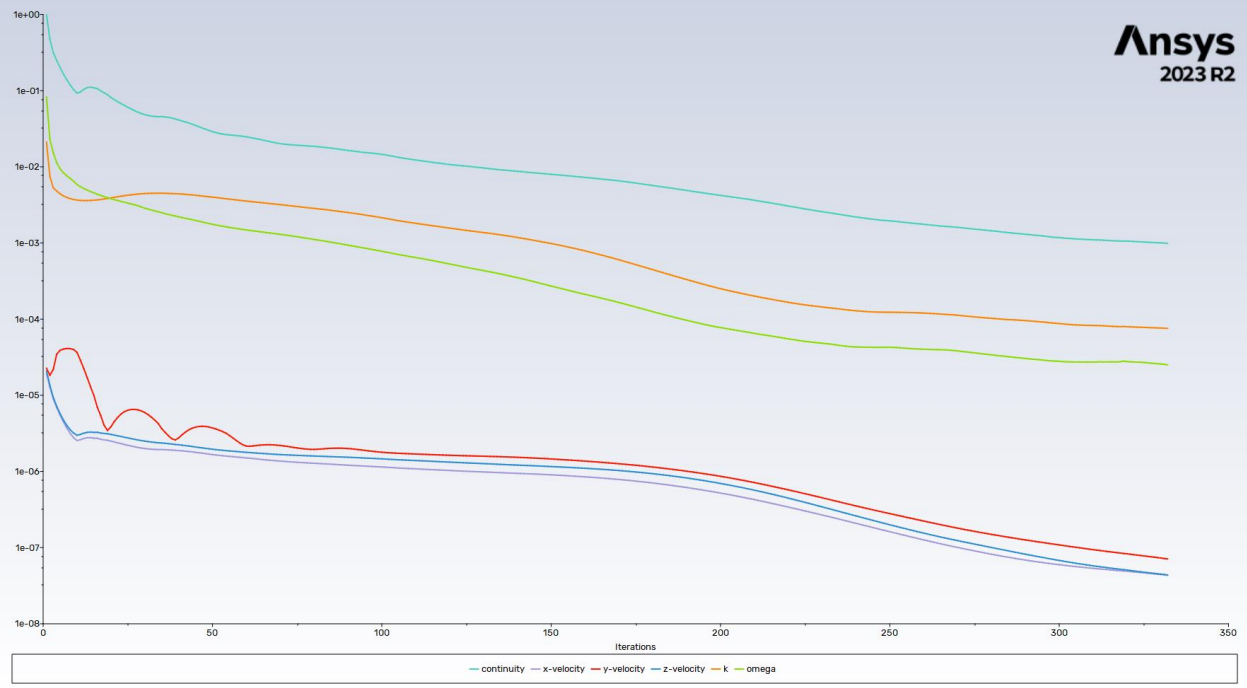


Figure 8: Output of residuals from ANSYS Fluent

Results:

Flow visualizations for all 5 angles of attack are shown in Fig. 9, with attack angle decreasing from left to right. These visualizations will be compared with the ANSYS simulations below. The angles are approximately 25°, 7°, 0°, and -11° respectively. The dye was injected in front of the leading edge of the patagium. In the 25° panel there is a clear separation between the stream of dye and the patagium. The dye flows over the model and then downwards to wrap around the trailing edge, indicating a leading-edge vortex. This vortex is also present in the 7° attack angle, but difficult to see due to the camera angle being underneath the patagium. The

remaining two attack angles do not show this separation. At the lowest angle, the dye stream glides smoothly over the patagium.



Figure 9: Flow visualizations showing fluid movement over patagium. Attack angles from left to right: 25°, 7°, 0°, and -11°.

ImageJ was used to measure the leading edge vortex and wake on the 25° attack angle [19]. The scale of the visualization was set in the software by drawing a line across a ruler attached to the flow tank. This allowed for ImageJ to output the numerical values by drawing lines across the vortex and wake. Multiple lines were drawn for each to achieve an average result. The leading edge vortex is 0.824 cm long and the wake is 4.269 cm. Since the model is the approximate size of a live specimen, these values do not need to be scaled.

ANSYS CFD Post was then used to visualize the simulations [11]. A 3D pressure contour of the 0° angle is first shown on the model in Fig 10. The gradient clearly shows regions of high and low pressure. This is consistent with generating lift force underneath the airfoil that is the patagium. Additionally, a high-pressure region on the tail shows that it is used as an air brake, consistent with my research.

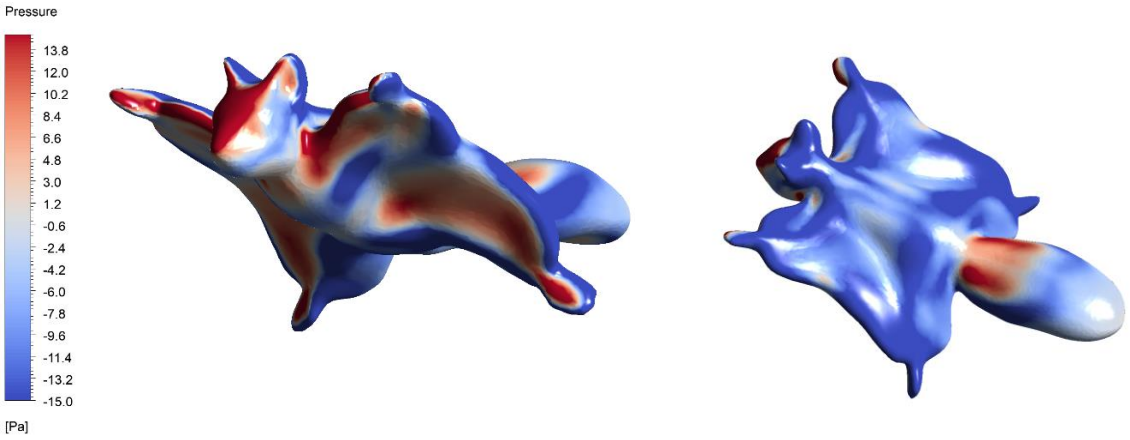


Figure 10: Pressure gradient on 3D model. Regions of high pressure shown below patagium in red. Low pressure regions are shown in blue. The same contour is shown in both camera angles.

Fig. 11 depicts a velocity vector map for the 0° attack angle. The vectors are placed on a 2D plane bisecting the squirrel. There is a clear low velocity region behind the squirrel, with velocity decreasing towards the upper right. This is indicative of a trailing high pressure region.

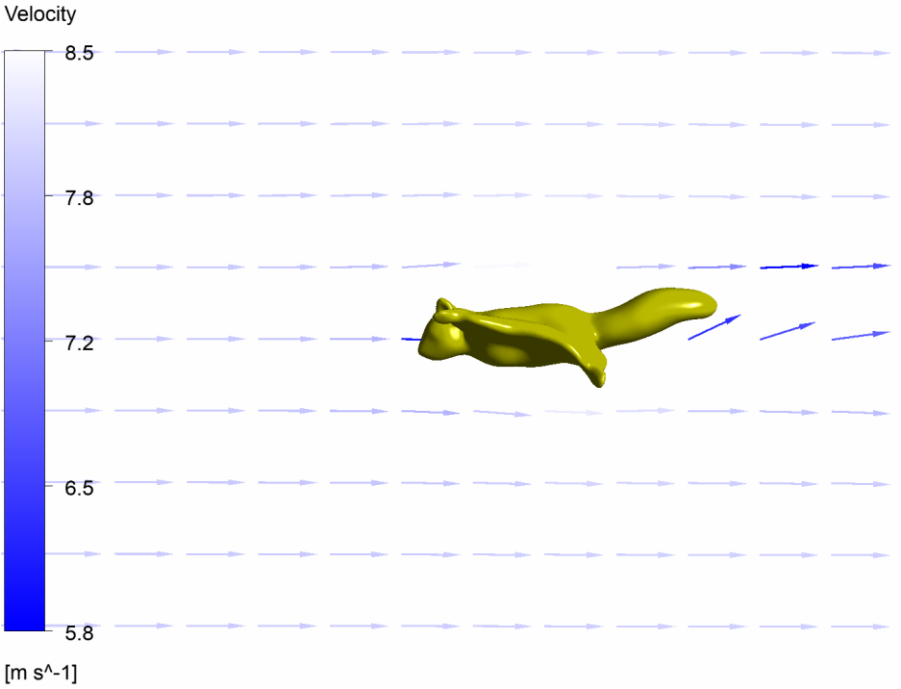


Figure 11: Velocity vectors mapped onto 2D plane bisecting the model. All vectors are the same size. Smaller velocities are shown in blue, whereas larger velocities are white.

The following two visualizations will show values for all three of the simulated attack angles. The velocity streamlines can be viewed below in Fig. 12. The streamlines were taken on a two-dimensional plane showing the widest cross section of the left patagium. All three streamlines show a region of relatively lower velocity behind the squirrel, consistent with the velocity contour in Fig 6. The leading edge vortex shown in the flow visualization can also be seen here in the 0° streamline. As the attack angle increases, the low velocity region grows in size. Furthermore, the difference between the highest and lowest velocity value is increased.

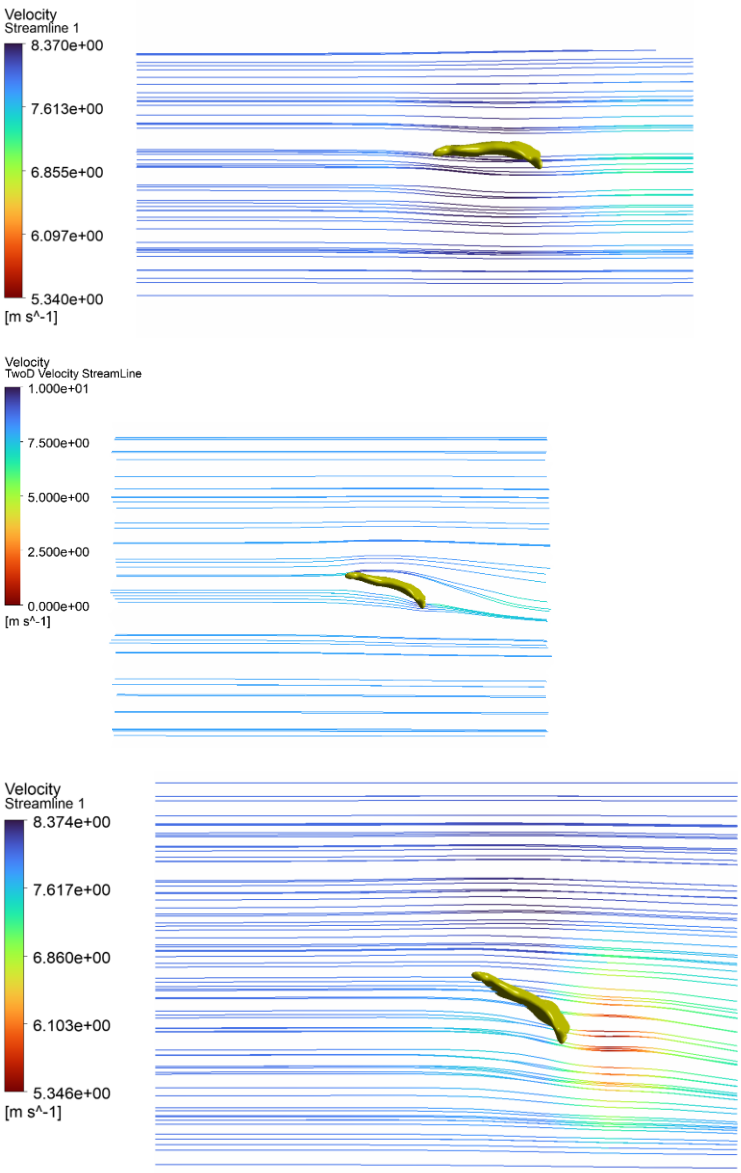


Figure 12: Velocity streamlines taken on 2D plane through patagium. Low velocity regions are shown in the red and yellow area behind the model. Angles are from top to bottom -15°, 0°, and 15°.

The out of plane vorticity for the model is shown in Fig. 13 on the same 2D plane as the above streamlines. There is a strong vortex in the plane of the patagium, indicating a region of

high drag. All three attack angles presented this high vorticity behind the squirrel. Increasing the angle of attack corelates with an increase in the magnitude of the vorticity.

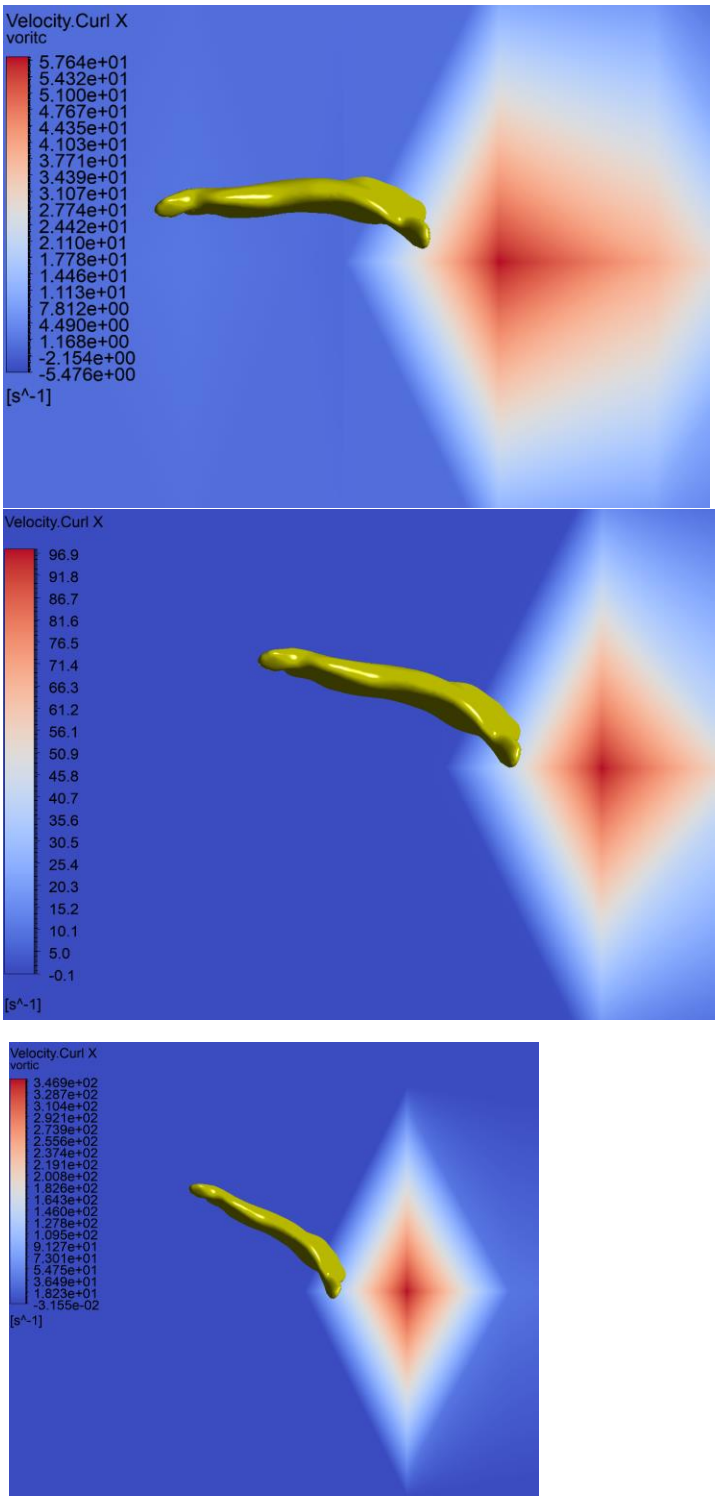


Figure 13: Out of plane vorticity for each angle of attack from top to bottomt: -15°, 0°, and 15°.

Lastly, the lift and drag forces and coefficients were quantitatively calculated within the ANSYS simulation [11]. I also found the ratio of lift and drag. The values are shown in the below table:

Angle of Attack	Drag Coefficient	Drag Force (N)	Lift Coefficient	Lift Force	L/D Ratio
-15	0.242	0.060	-0.181	-0.045	-0.749
0	0.264	0.065	0.268	0.066	1.018
15	0.483	0.119	0.753	0.186	1.559

A plot of the ratio vs attack angle is shown in Fig. 14:

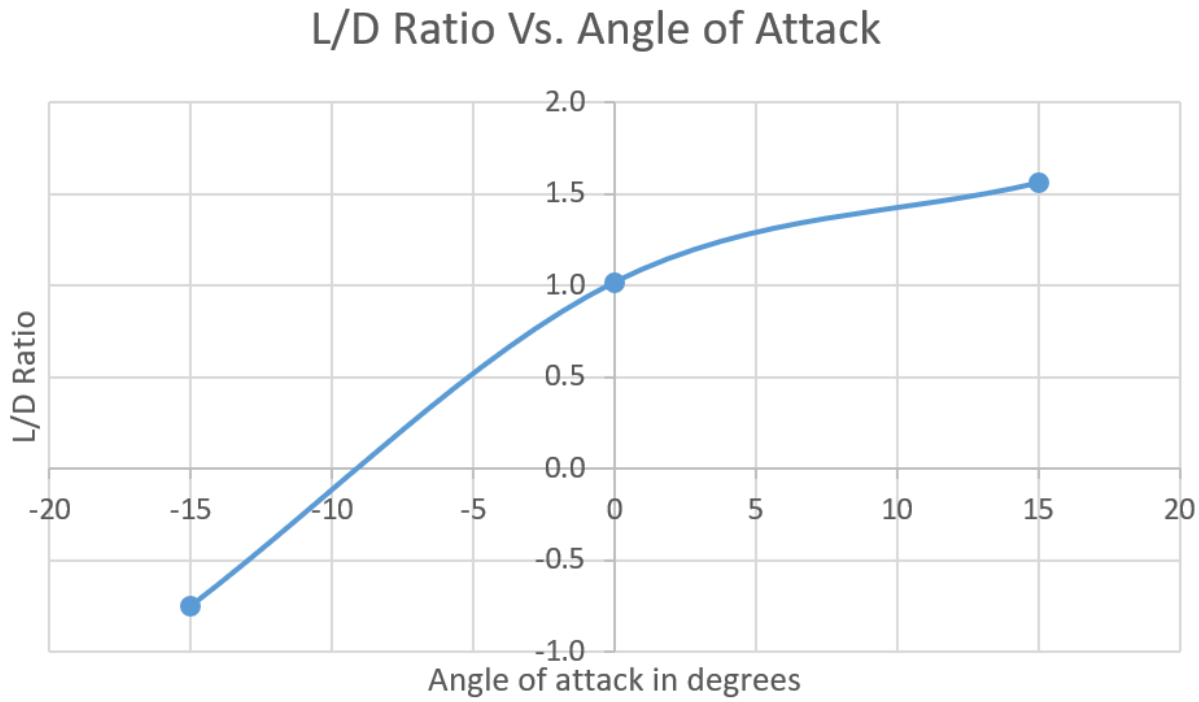


Figure 14: Plot of the lift to drag ratio Vs. the angle of attack. The L/D ration increases as the angle does.

There is a clear positive relationship between the lift-drag ratio and the angle of attack. This means that as the angle of attack is increased, the flying squirrel patagium experiences a stronger lift force and weaker drag force. The lift and drag forces are roughly equal at the 0° attack angle. Furthermore, a negative lift force is achieved at the negative 15° angle, implying that lower angles of attack increase the rate of descent during gliding.

Discussion:

The results from both the flow visualization and computational fluid dynamic simulations offer valuable insight into the aerodynamic effects of the northern flying squirrel's patagium. The dye visualization provided a clear qualitative assessment of the flow patterns at differing angles of attack. The leading-edge vortex and wake were particularly useful. The CFD simulations complemented this by quantitatively analyzing the impact of attack angles on lift and drag forces. A comparison of these two methods reveals a strong correlation between the observed flow patterns in the physical model and the simulated aerodynamic forces, underscoring the

reliability of the computational approach. However, the placement of the high vorticity region differs between the CFD model and the flow visualization. The flow tank showed high vorticity in the leading edge vortex, but the CFD model shows high vorticity in the region of airspace behind the squirrel. This is largely due to the inherent limitations of the flow tank, especially considering the different fluid properties between water and air.

The outcomes of these experiments relate closely to the initial hypothesis. As predicted, an increase in the angle of attack corelates with an increase in the lift coefficient. However, I am unable to identify the optimal range for aerodynamic performance. I am limited by the number of different attack angles that were simulated withing ANSYS [11]. Time constraints for this paper made it unrealistic to simulate more attack angles. In future studies I plan to increase the number of attack angles that are simulated. With a sufficient amount of data points a more useful plot of the lift-drag ratio can be made for the purpose of identifying the ideal attack angle for the gliding modality of robotics.

The study has further limitations, particularly in replicating exact real-world conditions in both the dye visualization and CFD simulations. The difference in environmental conditions between the experiments and natural settings could affect the generalizability of the results. This is especially so given the large discrepancy between the Reynold's number of the flow visualization and CFD. Additionally, the computational model, while detailed, still simplifies the Navier-Stokes equations with a different model.

Future work should aim at refining the experimental setup to more closely mimic real-world conditions. This could involve using more advanced visualization techniques and enhancing CFD models to include more complex fluid interactions. Further research could also explore different patagium shapes and textures to understand their impact on aerodynamic performance, expanding the scope of this study to a wider range of gliding animals and their biomimetic applications in robotics.

References

[1] Bishop, Kristin L. “The relationship between 3-D kinematics and gliding performance in the southern flying squirrel, *glaucomys volans*.” *Journal of Experimental Biology*, vol. 209, no. 4, 15 Feb. 2006, pp. 689–701, https://doi.org/10.1242/jeb.02062
[2] Li, X., Wang, W., Tang, Y., Wang, L., Bai, T., Zhao, F., & Bai, Y. (2018). Research on gliding aerodynamic effect of deformable membrane wing for a robotic flying squirrel. *Journal of Bionic Engineering*, *15*(2), 379–396. https://doi.org/10.1007/s42235-018-0029-5
[3] Li, Xuepeng, et al. "A research on air posture adjustment of flying squirrel inspired gliding robot." *2016 IEEE International Conference on Robotics and Biomimetics (ROBIO)*. IEEE, 2016.
[4] @Schlossbauer. “Flying Squirrel.” *Printables*, 3 Jan. 2022, https://www.printables.com/model/111836-flying-squirrel
[5] Yamamoto, Manabu, and Koji Isogai. "Direct measurement of unsteady fluid dynamic forces for a hovering dragonfly." *AIAA Journal* 43.12 (2005): 2475-2480.
[6] Zhao, F., Wang, W., Zhang, J., Wyrwa, J., & Sun, F. (2019). Aerodynamic characteristics and pitching adjusting mechanism of the flying squirrel with deployed patagium. *IEEE Access*, *7*, 185554–185564. https://doi.org/10.1109/access.2019.2961451
[7] Encyclopædia Britannica. *southern flying squirrel (Glaucomys volans)*. 27 May 1999, https://www.britannica.com/animal/flying-squirrel
[8] Bishop, Kristin L. “Aerodynamic force generation, performance and control of body orientation during gliding in sugar gliders (*petaurus breviceps*).” *Journal of Experimental Biology*, vol. 210, no. 15, 1 Aug. 2007, pp. 2593–2606, https://doi.org/10.1242/jeb.002071.
[9] Bahlman, Joseph W., et al. “Glide performance and aerodynamics of non-equilibrium glides in northern flying squirrels (*glaucomys sabrinus*).” *Journal of The Royal Society Interface*, vol. 10, no. 80, 6 Mar. 2013, p. 20120794, https://doi.org/10.1098/rsif.2012.0794.
[10] Thorington, Richard W., and Erica M. Santana. “How to make a flying squirrel:*glaucomys*anatomy in phylogenetic perspective.” *Journal of Mammalogy*, vol. 88, no. 4, 20 Aug. 2007, pp. 882–896, https://doi.org/10.1644/06-mamm-s-325r2.1.
[11] ANSYS Student Edition version 2023 R2, https://www.ansys.com/academic/students/ansys-student
[12] Autodesk Meshmixer, https://meshmixer.com/
[13] PREZIOSO, Domenico, et al. “Ion specificity in determining physico-chemical properties of drinking water.” *Food Science and Technology*, vol. 39, no. 2, June 2019, pp. 485–490, https://doi.org/10.1590/fst.34717.
[14] Kestin, Joseph, et al. “Viscosity of liquid water in the range −8 °C to 150 °C.” *Journal of Physical and Chemical Reference Data*, vol. 7, no. 3, 1 July 1978, pp. 941–948, https://doi.org/10.1063/1.555581.
[15] Leutenegger, Stefan, et al. “Flying Robots.” *Springer Handbook of Robotics*, 2016, pp. 623–670, https://doi.org/10.1007/978-3-319-32552-1_26.
[16] Autodesk Inventor, https://www.autodesk.com/products/inventor/overview
[17] Bambu Studio, https://bambulab.com/en/download/studio
[18] Vogel, Steven, and Michael LaBarbera. “Simple flow tanks for research and teaching.” *BioScience*, vol. 28, no. 10, Oct. 1978, pp. 638–643, https://doi.org/10.2307/1307394.
[19] ImageJ, https://imagej.net/ij/download.html